Localization dynamics of excitons in disordered semiconductor quantum wells

Rohan Singh,[1,2,3,*] Marten Richter,[4] Galan Moody,[1,2] Mark E. Siemens,[5] Hebin Li,[6] and Steven T. Cundiff[1,2,3,†]

[1]*JILA, University of Colorado & National Institute of Standards and Technology, Boulder, Colorado 80309-0440, USA*

[2]*Department of Physics, University of Colorado, Boulder, Colorado 80309-0390, USA*

[3]*Department of Physics, University of Michigan, Ann Arbor, Michigan 48105-1040, USA*

[4]*Institut für Theoretische Physik, Nichtlineare Optik, und Quantenelektronik, Technische Universität Berlin, 10623 Berlin, Germany*

[5]*Department of Physics and Astronomy, University of Denver, Denver, Colorado 80208-6900, USA*

[6]*Department of Physics, Florida International University, Miami, Florida 33199, USA*

(Received 22 July 2016; published 23 June 2017)

Exciton transport in nanomaterials is sensitive to fluctuations in the confinement potential that are intrinsic to heterogeneous solid-state systems. Redistribution of exciton population manifests as spectral diffusion in which the exciton energy shifts. It is generally assumed that increase or decrease in the exciton energy are equally probable. We show that this assumption is not necessarily valid using two-dimensional coherent spectroscopy on a disordered GaAs quantum well. High-energy excitons relax into lower-energy localized states over a time scale of tens of picoseconds at low sample temperatures (∼5 K). A transition to uniform spectral diffusion of excitons is observed as the temperature is increased to ∼20 K. Numerical simulations reveal the contribution of exciton-phonon interactions to spectral diffusion of excitons. These results provide a perspective on the process of dynamic localization and the effect of the correlation length of disorder on spectral diffusion of excitons.

DOI: 10.1103/PhysRevB.95.235307

I. INTRODUCTION

The transport of optically created excitations in nanostructures [1–3] is critical for optoelectronics applications such as light harvesting [4,5], light-emitting diodes [6,7], optical modulators [8], and switches [9,10]. Transport properties are affected by unavoidable structural disorder, which introduces varying local potentials that spatially confine charge carriers, resulting in a decrease in carrier mobility. For example, carriers can be localized due to the interface roughness of a quantum well (QW) confining a two-dimensional electron gas (2DEG) [11], surface trap states in a colloidal quantum dot (CQD) and perovskite films [12–14], or crystal impurities in transition-metal dichalcogenides (TMDs) [15]. Understanding the carrier localization dynamics in heterogeneous solid-state systems is critical for the aforementioned applications, but isolating these dynamics from other physical phenomena can be difficult. In the case of 2DEGs, the effect of surface roughness is obscured by strong Coulomb interactions between electrons. In CQD and perovskite films, the surface trap states are optically dark, inhibiting the ability to probe the trapping dynamics.

Excitons, which are correlated electron-hole pair excitations, in disordered QWs are a model system to study localization without being constrained by the limitations mentioned above. The exciton resonance is inhomogeneously broadened by spatial variations in the confinement potential due to spatial disorder in the width [16] or chemical composition [17] of the QW. Spatial motion of excitons results in dynamic fluctuations of their energy, which is known as spectral diffusion [18]. Low-energy excitons are spatially localized in the lateral direction [19,20] while high-energy excitons are delocalized in the plane of the QW. The exciton energy at which the transition from localized to delocalized states occurs is dubbed the mobility edge [21,22]. Thus, the dynamic localization of high-energy "mobile" excitons will decrease their transition energy. Unlike the trap states in CQDs, both localized and delocalized excitons are optically bright, which facilitates measurement of their energy change. As neutral quasiparticles, they are less susceptible to Coulomb scattering compared to carriers in a 2DEG. A disordered QW is also an excellent system to model exciton diffusion in layered materials such as TMDs [15] and perovskites [23], which exhibit similar excitonic phenomena and are more susceptible to interactions with the surrounding environment.

Spectral diffusion of excitons in QWs has been studied with the goal of understanding transport of neutral particles for more than three decades [18]. Several experimental techniques such as frequency-domain four-wave mixing (FWM) [24] and three-pulse photon echo peak shift (3PEPS) [25,26] have been used. Regardless of the system under study, the time-domain experiments measure the decrease in the frequency-frequency correlation function [27] as a function of time [28]. Measurement of the correlation function is sufficient to understand the energy fluctuations in the limit of equally probable fluctuations to higher and lower energies, which is the strong-redistribution approximation (SRA) [24]. This approximation correctly describes the non-Markovian decay dynamics in atoms [29,30], solvation dynamics of molecules [31,32], and fluctuating electric fields around single quantum dots [33,34]. However, in the case of heterogeneous systems such as excitons in a QW, static inhomogeneity increases the complexity. Localized and delocalized excitons, in fact, show different spectral diffusion characteristics in frequency-domain experiments performed on a QW with sample temperature below 5 K [35], which suggests that the SRA is not necessarily valid. However, until the advent of two-dimensional coherent spectroscopy (2DCS), experimental techniques were not able to clearly show that the SRA was invalid. Recently, the validity of the SRA was experimentally demonstrated for temperatures above ∼30 K

*Present address: Chemistry Division, Los Alamos National Laboratory, Los Alamos, New Mexico 87545, USA.

†cundiff@umich.edu

[36]. Nevertheless, the SRA has been implicitly assumed when interpreting the decay of the correlation function of excitons in QWs measured from the time-domain studies even for lower temperatures [25,26,37]. In the frequency domain, on the other hand, only the steady-state population distribution has been accessible, which conceals all the relevant localization and diffusion dynamics.

In this paper, we present measurements of spectral diffusion of excitons in disordered QWs using 2DCS, which has been previously used for spectral diffusion studies of vibrational and electronic excitations in molecular systems [38,39], and to quantify spectral diffusion of excitons in QWs for sample temperatures above 30 K [36]. Spectrally resolved exciton diffusion dynamics are measured for the entire inhomogeneously broadened distribution simultaneously. We observe that the SRA fails for a sample temperature around 5 K due to preferential relaxation of more delocalized excitons to the lower-energy localized states. This dynamic localization occurs over a time scale of tens of picoseconds. A theoretical formalism describing 2DCS measurements of spectral diffusion of excitons in disordered QWs is presented. Comparison between experiment and simulations reveals the role of acoustic phonons in spectral diffusion of excitons. A transition to spectral diffusion that is well described with the SRA is observed as the sample temperature is increased, which is attributed to an increase in the population of acoustic phonons.

The rest of the paper is organized as follows. The theoretical formalism of calculating the excitonic properties in a disordered QW is discussed in Sec. II. Section III discusses the experimental and theoretical details of 2DCS. The results and their discussion are presented in Sec. IV, which highlights the spectral diffusion behavior apparent in 2D spectra and changes in exciton population distribution through Green's function. We also discuss the process of dynamic localization and the effect of disorder correlation length on the spectral diffusion process.

II. THEORY

In this section we give an overview of the theoretical approach to treat excitons in a disordered QW and its interaction with light. To overcome the limitations of previous theoretical studies of excitonic spectral diffusion in QWs, we use a microscopic model that includes calculations of the exciton transition strength, rates of the exciton-phonon scattering processes, and the exciton radiative lifetime. The theory is similar to the framework developed in Refs. [40,41] to describe the photoluminescence dynamics of $1s$ excitons in QWs in the presence of disorder. In the first subsection, we will introduce the theoretical model for obtaining the exciton wave function, including the treatment of disorder. The second subsection discusses scattering processes such as exciton-phonon interaction, exciton recombination, and the overall dynamics of density matrix elements such as exciton coherences and populations.

A. Exciton states in disordered quantum wells

The two-dimensional exciton wave function $\Psi(\boldsymbol{\rho}_e,\boldsymbol{\rho}_h)$, which describes the excitons states, is a solution to the stationary two-dimensional Schrödinger equation

$$E\Psi(\boldsymbol{\rho}_e,\boldsymbol{\rho}_h)=\Big[-\frac{\hbar^2\nabla_e^2}{2m_e}-\frac{\hbar^2\nabla_h^2}{2m_h}+V_{eh}(\boldsymbol{\rho}_e-\boldsymbol{\rho}_h)+V_h(\boldsymbol{\rho}_h)+V_e(\boldsymbol{\rho}_e)\Big]\Psi(\boldsymbol{\rho}_e,\boldsymbol{\rho}_h), \tag{1}$$

where E is the energy of the exciton, ∇_i^2 $(i=e,h)$ is the Laplacian operator for the position, m_i is the effective mass, $\boldsymbol{\rho}_i$ is the coordinate in the plane of the QW, V_i is the confinement potential, and V_{eh} is the electron-hole Coulomb-interaction potential. We use subscripts e and h to denote electrons and holes, respectively, throughout this paper. As is usual in the envelope approximation, V_{eh} is modified by the envelope functions $\zeta_i(z_i)$ in the z direction, which is perpendicular to the plane of the QW, as

$$V_{eh}(\rho)=-\frac{e^2}{4\pi\varepsilon_0\varepsilon_r}\int dz_e\int dz_h\frac{\zeta_e^*(z_e)\zeta_h^*(z_h)\zeta_h(z_h)\zeta_e(z_e)}{\sqrt{\rho^2+(z_e-z_h)^2}}, \tag{2}$$

where e is the electron charge, ε_0 is the vacuum permittivity, and ε_r is the relative permittivity. The envelope functions are obtained from the equation

$$\Big[-\frac{\hbar^2\partial_{z_i}}{2m_i}+V_{\mathrm{con},i}(z_i)\Big]\zeta_i(z_i)=E_i\zeta_i(z_i), \tag{3}$$

where we assumed an infinite potential well of width $L_w=10$ nm for the confinement potentials $V_{\mathrm{con},i}(z_i)$. Since an infinite potential well is assumed, in principle, an effective QW width has to be used for a direct comparison with a finite potential well in the experiment. However, for the internal dynamics of the $1s$-exciton state, which is considered here, this detail is of minor importance and has been ignored in our calculations.

In order to account for disorder due to the spatial fluctuations in the QW width, the confinement potentials $V_e(\boldsymbol{\rho}_e)$ and $V_h(\boldsymbol{\rho}_h)$ are spatially disordered. The variations in the interface-width $w(\boldsymbol{\rho})$ are characterized by thickness fluctuations (with mean deviation $\Delta w=0.19$ nm, adjusted to match the inhomogeneous distribution in the experiment). This thickness fluctuation corresponds to a disorder of $\sim$1.8 meV in the exciton confinement potential. The correlation length ξ of the spatial fluctuation of the QW width is defined as $\langle w(\boldsymbol{\rho})w(\boldsymbol{\rho}')\rangle=\alpha^2\exp[-|\boldsymbol{\rho}-\boldsymbol{\rho}'|/(2\xi^2)]$, where α is an arbitrary constant (cf. Ref. [40]). Unless otherwise stated, we set the correlation length ξ to 20 nm. The disorder potentials for electron and hole are both proportional to $w(\boldsymbol{\rho})$, yielding $V_i(\boldsymbol{\rho})\propto w(\boldsymbol{\rho})$. The proportionality factor is extracted by taking the first-order contribution of a Taylor expansion of the subband energy E_e or E_h. All calculations are repeated for different random realizations of the disorder potential and the resulting spectra are averaged in the end. Since obtaining $\Psi(\boldsymbol{\rho}_e,\boldsymbol{\rho}_h)$ requires the solution of a four-dimensional partial differential equation, we use the approximation of factorizing the relative motion of electron and hole from the center-of-mass (COM) motion of the exciton: $\Psi(\boldsymbol{\rho}_e,\boldsymbol{\rho}_h)=\psi(\mathbf{R})\phi(\mathbf{r})$ with the COM coordinate $\mathbf{R}=(m_e\boldsymbol{\rho}_e+m_h\boldsymbol{\rho}_h)/(m_e+m_h)$ and the relative coordinate $\mathbf{r}=\boldsymbol{\rho}_h-\boldsymbol{\rho}_e$. First, the Wannier

equation for the relative part of the wave function,

$$E\phi(\mathbf{r}) = \left[-\frac{\hbar^2\nabla_{\mathbf{r}}^2}{2m_r} + V_{eh}(\mathbf{r})\right]\phi(\mathbf{r}), \tag{4}$$

is solved numerically using the Petsc [42–44] and Slepc [45] libraries using finite differences for approximating the differential operators [46]. Here, $1/m_r = 1/m_e + 1/m_h$. Since the important dynamics in the experiment are associated with the $1s$-exciton state and the other states are energetically well separated, only $1s$-like exciton solutions are included in the theoretical framework. After this, the COM wave function $\psi(\mathbf{R})$ of the $1s$ exciton is obtained using the Schrödinger equation of the COM wave function

$$E\psi(\mathbf{R}) = \left[-\frac{\hbar^2\nabla_{\mathbf{R}}^2}{2M} + V_{\text{dis}}(\mathbf{R})\right]\psi(\mathbf{R}), \tag{5}$$

with $M = m_e + m_h$ and the effective disorder potential for the $1s$ state

$$V_{\text{dis}}(\mathbf{R}) = \int d\mathbf{r}|\phi(\mathbf{r})|_{1s}^2\left[V_e\left(\mathbf{R} - \frac{m_h}{M}\mathbf{r}\right) + V_h\left(\mathbf{R} + \frac{m_e}{M}\mathbf{r}\right)\right]. \tag{6}$$

We calculated the 2500 lowest COM eigenstates, for a 409.6 nm × 409.6 nm computational domain, which includes the bright-exciton COM states as well as a sufficient number of dark states for describing a realistic exciton-phonon interaction. Properties obtained from the microscopic calculation, such as the homogeneous broadening of individual states, differ in each random realization. Since the spectroscopic signal depends on these parameters, we average it over multiple realizations (usually 40–50). Note that the excitation spot in the experiment is ∼50 μm, which is significantly larger than the computational area.

Figure 1 shows the results of the calculation of the excitonic properties after averaging over random realizations of the disorder potential. Since the band-gap energy does not enter the calculation of the exciton states, the exciton energy in Fig. 1(a), and in the successive plots, includes an offset to

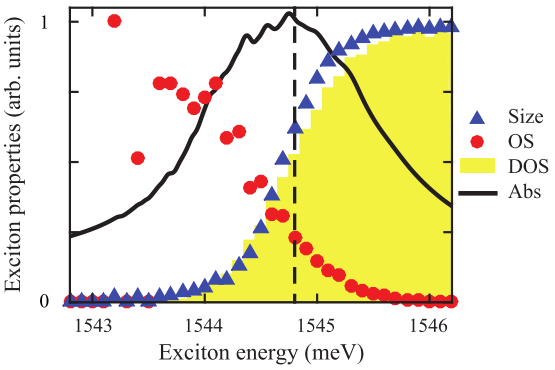

FIG. 1. Calculated $1s$-exciton properties as a function of exciton energy. The exciton density of states (DOS) is plotted as a bar graph. The absorption spectrum (Abs), oscillator strength (OS), and exciton wave function size (Size) are also plotted. The approximate mobility-edge energy is indicated by the dashed line.

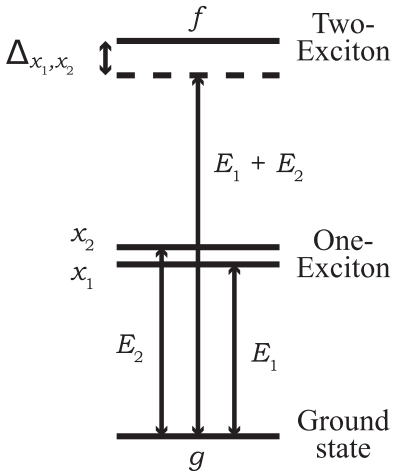

FIG. 2. Energy level of $1s$-exciton states showing the ground (g), one-exciton (x_1 and x_2), and two-exciton (f) states. One-exciton states x_1 and x_2 have energies E_1 and E_2, respectively. The two-exciton state f has energy $E_1 + E_2 + \Delta_{x_1,x_2}$, where Δ_{x_1,x_2} is the interaction energy between excitons x_1 and x_2.

match the experimental data. The size of the wave function ψ is defined as $\sqrt{\langle(\mathbf{R} - \langle\mathbf{R}\rangle)^2\rangle}$ with some adjustments for the periodic computational area. The maximum wave function size is limited by the chosen lateral dimension of the QW, and increases with exciton energy as the exciton transitions from being localized to delocalized at the mobility edge [dashed line in Fig. 1(a)], which is estimated from the experimental data presented later. The oscillator strength (OS) decreases with increase in exciton energy, which means that the delocalized excitons are optically "darker" compared to the localized excitons. At the same time, the density of states (DOS) of the delocalized excitons is significantly higher than that of the localized excitons. As a result, the exciton absorption spectrum, which is roughly equivalent to the product of the OS and DOS, peaks near the mobility edge.

B. Scattering processes and equation of motion for the density matrix

The excitonic states relevant to the calculations are shown in Fig. 2. The energy-level scheme shows the unexcited (ground) state g, the one-exciton states x, and two-exciton states f, which may be excited by the absorption of two photons. This two-exciton state comprises two independent excitons with different COM states. For instance, Fig. 2 shows one-exciton states x_1 and x_2 forming the two-exciton state f. The creation of a second exciton at the same disorder position wave function (a bound biexciton) is prevented by the cocircular excitation of the sample in the experiment [47], and has been ignored in the theory. The energy of the single-exciton state x is E_x. In general, the energy of a two-exciton state f that is composed of single excitons x_1 and x_2 is $E_{f_{12}} = E_{x_1} + E_{x_2} + \Delta_{x_1,x_2}$, with an exciton-exciton interaction strength of Δ_{x_1,x_2} (this may result from the first-order perturbation theory with respect to the two-exciton states). As will be discussed later, from the experimental results we conclude that Δ_{x_1,x_2} is negligible

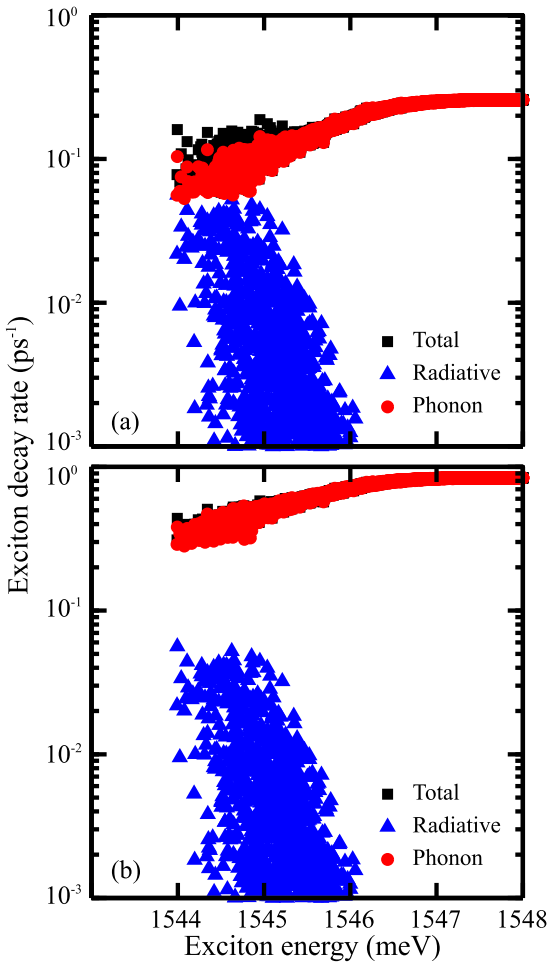

FIG. 3. Calculated exciton decay rates as a function of the exciton energy for sample temperatures of (a) 5 K and (b) 20 K. The plot shows the total decay rate (black squares) and its radiative (blue triangles) and phonon-scattering (red circles) components. The decay rates for exciton states from 10 random realizations are shown.

for the photon-echo experiment and we can safely assume $\Delta_{x_1,x_2} \approx 0$ [48].

In order to model the evolution of excitonic population distribution we need to consider the dynamics of the various density matrix elements, which describe the inhomogeneous exciton system, without the influence of the exciton-light interaction. These dynamics are driven by two types of scattering processes: exciton-phonon scattering and radiative exciton recombination. The exciton-phonon scattering rate $\gamma_{x\to x'}$ describes the process where an exciton in COM state x is converted to another exciton state x' through the emission or absorption of a phonon. The radiative rate r_x, on the other hand, describes the electron-hole recombination processes accompanied by the emission of a photon. Both the scattering rates are calculated using the formulas listed in Appendix A. Figures 3(a) and 3(b) show the calculated decay rates for sample temperature of 5 and 20 K, respectively. The total exciton decay rate out of state x due to exciton-phonon scattering is calculated through the summation $\sum_{x'\neq x}\gamma_{x\to x'}$. We find that the radiative decay rate gets smaller with an increase in exciton energy, which is expected from the calculation of the oscillator strength shown in Fig. 1. The contribution due to the exciton-phonon processes, on the other hand, increases with increase in energy and eventually saturates around 1546 meV. A consequence of this behavior is that the radiative processes have a significant contribution to the exciton decay rate only for the localized states. Furthermore, since the radiative decay of a particular state is almost independent of the temperature, the relative contribution of radiative decay is diminished with increasing temperature because the exciton-phonon scattering rate increases due to an increase in the phonon population. These results are similar to that shown in Fig. 4.5 in Ref. [41].

Based on these scattering rates, we can define dephasing rates for the single- and double-exciton states as $\gamma_x = \frac{1}{2}(r_x + \sum_{x'\neq x}\gamma_{x\to x'})$ and $\gamma_f = \gamma_{x_1} + \gamma_{x_2}$, respectively, which are used to calculate the evolution of various density matrix elements. The ground to one-exciton coherences obey the dynamics

$$\partial_t \rho_{xg} = -\imath[E_x - E_g - \imath\gamma_x]\rho_{xg}. \tag{7}$$

This dynamics is similar to the two-exciton to ground state coherence for f consisting of x_1 and x_2:

$$\partial_t \rho_{fg} = -\imath[E_f - E_g - \imath\gamma_f]\rho_{fg}. \tag{8}$$

The dynamics of exciton coherences $\rho_{xx'}$ (with $x \neq x'$) are given by

$$\partial_t \rho_{xx'} = -\imath[E_x - E_{x'} - \imath(\gamma_x + \gamma_{x'})]\rho_{xx'}. \tag{9}$$

The decay of exciton population ρ_{xx} in state x follows the rate equation

$$\partial_t \rho_{xx} = -2\gamma_x \rho_{xx} + \sum_{\tilde{x}} \gamma_{\tilde{x}\to x}\rho_{\tilde{x}\tilde{x}}. \tag{10}$$

The rate of change of population in the ground state ρ_{gg} is related to the radiative decay of the excited states as

$$\partial_t \rho_{gg} = \sum_x r_x \rho_{xx}. \tag{11}$$

We define a relaxation tensor $\Gamma_{x\tilde{x}}$ and reformulate the above equations, which describe the population evolutions, in the form

$$\partial_t \rho_{xx} = \sum_{\tilde{x}} \Gamma_{x\tilde{x}}\rho_{\tilde{x}\tilde{x}}, \tag{12}$$

and define the Green's function $G_{xx'}(t_1,t_2)$ with $G_{xx'}(t_1,t_1) = \delta_{xx'}$, where δ is the Kronecker delta and

$$\partial_t G_{xx'}(t_1,t) = \sum_{\tilde{x}} \Gamma_{x'\tilde{x}} G_{x\tilde{x}}(t_1,t). \tag{13}$$

The Green's function $G_{xx'}(t,t_1)$ is basically the probability that an exciton in state x at time t_1 ends up in state x' at time t. The Green's function will be used later for calculating the contributions of the different Liouville diagrams (see Appendix B). The Green's function plots presented later can be related to $G_{xx'}(t_1,t_2)$ through the relation

$$G(E_f, E_i = \omega_{xg}; T) = \sum_{x'} G_{xx'}(T)\delta(E_f = \omega_{x'g}), \tag{14}$$

where E_i and E_f are the initial and final exciton energy, respectively.

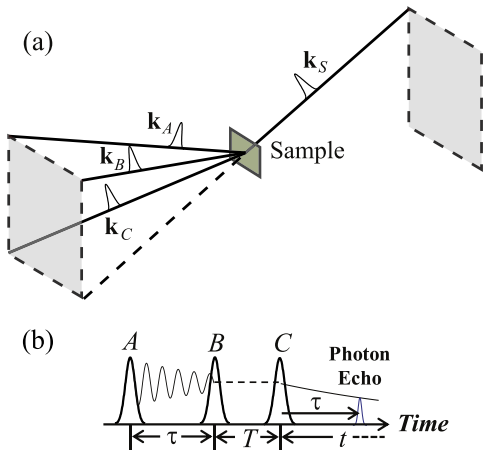

FIG. 4. (a) Schematic of the experimental setup. Pulses A, B, and C are incident on the sample with wave vectors $\mathbf{k}_A$, $\mathbf{k}_B$, and $\mathbf{k}_C$, respectively. The FWM signal is emitted in the phase-matched direction $\mathbf{k}_S$. (b) Pulse timing for our 2DCS experiment. Excitation pulses A, B, and C are separated by delays τ and T in the rephasing time ordering. The signal is emitted during time t as a photon echo.

III. TWO-DIMENSIONAL COHERENT SPECTROSCOPY

To study spectral diffusion dynamics of excitons in QWs without the need to invoke the SRA, we used optical 2DCS. In this section we describe the experimental procedure and the simulation technique.

A. Experiment

2DCS is similar to a three-pulse FWM experiment with the addition of phase-stabilized delay between the excitation pulses and detection of the signal field [49]. Figure 4(a) depicts the actively phase-stabilized excitation pulses A, B, and C incident on the sample with wave vectors $\mathbf{k}_A$, $\mathbf{k}_B$, and $\mathbf{k}_C$, respectively. The signal is detected along the phase-matched direction $\mathbf{k}_S = -\mathbf{k}_A + \mathbf{k}_B + \mathbf{k}_C$. The excitation scheme in Fig. 4(b) shows excitation pulses A, B, and C separated by time intervals τ and T, respectively. This pulse sequence is the rephasing time-ordering with the so-called conjugated pulse A being the first pulse that is incident on the sample. As a result, the FWM signal is emitted during time t as a photon echo due to inhomogeneous broadening. This signal is heterodyned with a reference pulse and detected through spectral interferometry, which allows us to measure both the amplitude and phase of the FWM signal. In a typical 2DCS experiment, the spectrally resolved FWM signal field is recorded as delay τ is scanned, while keeping delay T constant. A 2D spectrum is obtained by taking a numerical Fourier transform of the signal with respect to delay τ. 2D spectra are recorded for different values of T, during which the exciton population can evolve incoherently. The fluctuation of exciton energies during this incoherent evolution results in spectral diffusion. As will be discussed later, dynamic evolution of the peak line shape in the 2D spectrum informs on the changes in the population distribution of excitons. This experiment is identical to that used to study incoherent coupling between spectrally separated excitonic states in a QW and quantum dots [50]. All the excitation pulses and the radiated signal are

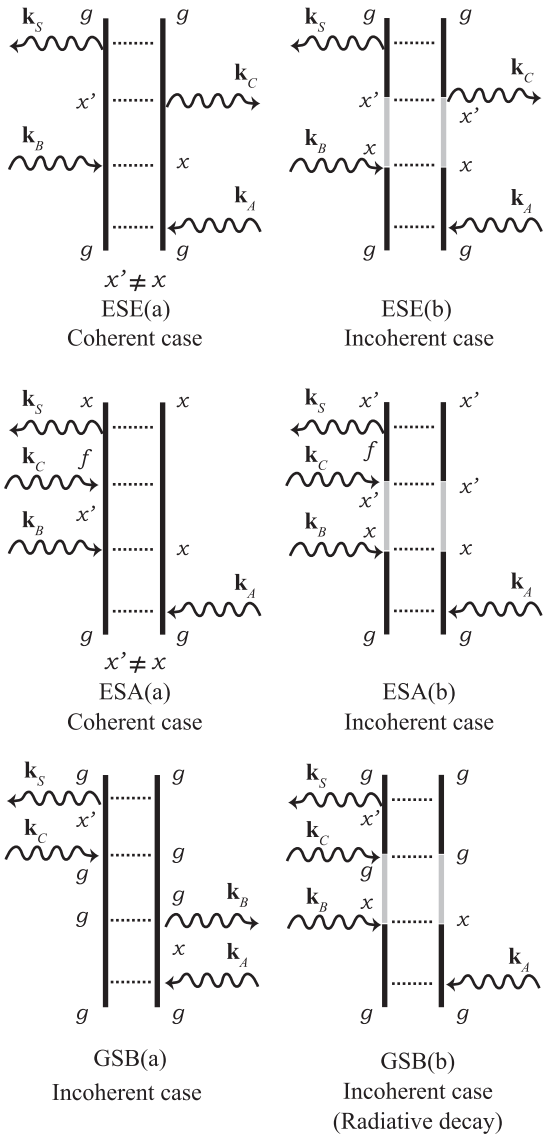

FIG. 5. The Liouville pathways that contribute to the photon-echo signal including the coherent and incoherent excited state emission (ESE), excited state absorption (ESA), and ground state bleach (GSB) pathways. $\mathbf{k}_A$, $\mathbf{k}_B$, and $\mathbf{k}_C$ are the wave vectors of the incident pulses; $\mathbf{k}_S$ is the wave vector of the emitted photon-echo signal.

cocircularly polarized so that the bound biexciton state is not excited [47]. The experiments were performed on a four-period 10-nm-wide GaAs QW sample with 10-nm-wide $Al_{0.3}Ga_{0.7}As$ barriers. Only the heavy hole (HH) exciton resonance was excited with ∼150-fs-long pulses. The sample was held in a sample-in-vapor helium flow cryostat. The experiment was repeated for sample temperatures between 5–20 K.

B. Simulation

We use a sum-over-states treatment of the spectroscopic signals analogous to Ref. [51] to calculate 2D spectra for comparison with experiments. The relevant states are the (unexcited) ground g, exciton x, and two-exciton states f, as described in Sec. II B. The FWM signal can be separated into the Liouville diagrams shown in Fig. 5. Similarly to Ref. [51],

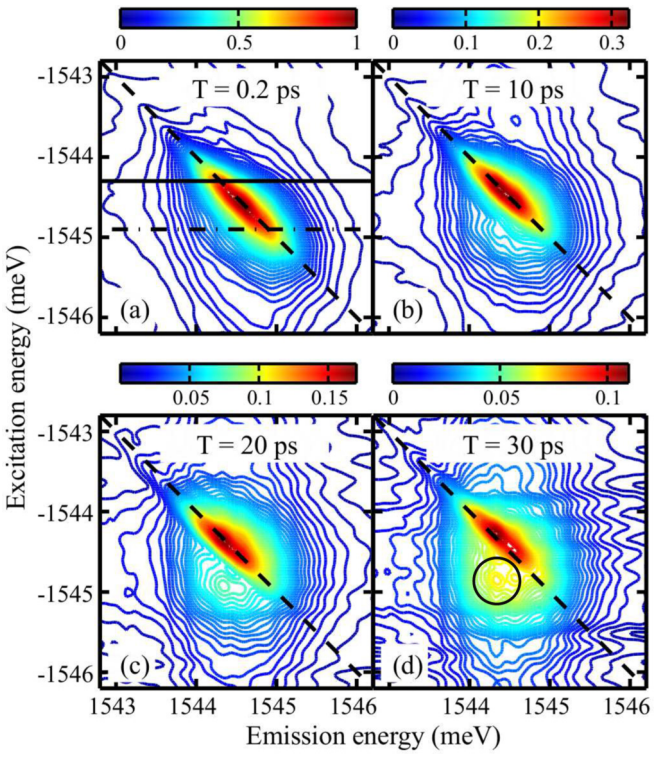

FIG. 6. (a)–(d) Experimental 2D spectra for $T = 0.2$, 10, 20, and 30 ps, respectively, with the sample at a temperature of 5 K. All the spectra are normalized by the maximum of the peak of the spectrum for $T = 0.2$ ps. The horizontal lines in (a) indicate excitation energies for the slices shown in Fig. 8. Note the relative increase in the signal within the circled region in (d).

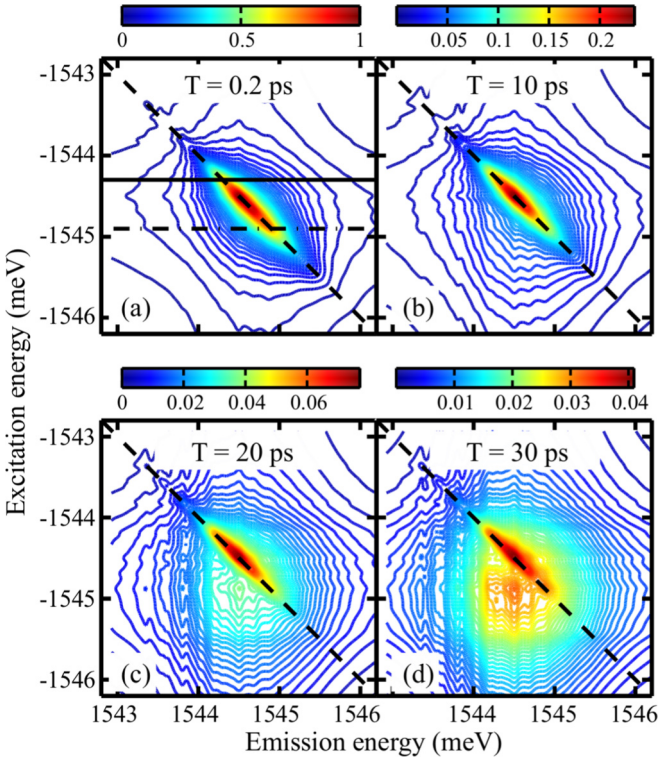

FIG. 7. (a)–(d) Simulated 2D spectra for $T = 0.2$, 10, 20, and 30 ps, respectively, with the sample at a temperature of 5 K. All the spectra are normalized by the maximum of the peak of the spectrum for $T = 0.2$ ps. The horizontal lines in (a) indicate excitation energies for the slices shown in Fig. 8.

we have contributions from the pathways which are referred to as excited state emission (ESE), excited state absorption (ESA), and ground state bleaching (GSB). Both ESE and ESA can be separated into pathways that are coherent and incoherent during delay T [51]. In the case of incoherent pathways, the population relaxation is included using the Green's functions of the rate equations. However, in QWs the radiative decay is on a time scale similar to that of the relaxation induced by exciton-phonon scattering. Therefore, the entire exciton population in the sample just after the second pulse is incident does not stay in the population state when the third pulse is incident on the sample. Consequently, we have to include the process where the exciton population radiatively decays to the ground state during delay T. This process is described by the GSB (b) diagram in Fig. 5.

The overall signal $S_{\mathbf{k}_I}(\Omega_3, T, \Omega_1)$ is obtained by summing over all the contributions from the pathways shown in Fig. 5. The contributions of the individual pathways are listed in Appendix B. The excitation and emission frequency variables Ω_1, Ω_3 are obtained by taking a Fourier transform of the signal along the time delays τ and t, respectively.

IV. RESULTS AND DISCUSSION

Having discussed the experimental and theoretical tools that we have used in this work, we will present our findings in this section.

A. 2D spectra

We begin by discussing the spectral diffusion of excitons, as seen in 2D spectra. Figure 6 shows the measured absolute-value 2D spectra with T ranging from 0.2–30 ps for a sample temperature of 5 K. The excitation energy is negative to indicate that the phase evolution during delay τ is opposite to that during t for the rephasing time-ordering. The peak is elongated along the dashed diagonal line due to inhomogeneous broadening of the HH 1s-exciton resonance due to the disordered confinement potential. The absence of off-diagonal features indicates that the contribution from a doubly excited state, formed due to interactions between two excitons in different COM states, can be neglected ($\Delta_{x_1,x_2} \approx 0$). The decay of the total signal strength due to population relaxation is accompanied by a change in the peak shape as T increases. The peak shape for a delay T tell us about the population distribution of the excitons. Thus the change in the peak shape reflects evolution in the population distribution due to spectral diffusion caused by exciton-phonon scattering between the different localized and delocalized 1s-exciton states. As delay T increases, the signal appears below the diagonal in the circled region in Fig. 6(d) due to a preferential relaxation of excitons from the high-energy, more delocalized states to the low-energy, more localized states. Energy conservation requires that this dynamic localization be accompanied by stimulated or spontaneous emission of acoustic phonons. These data show that the dynamic localization occurs over

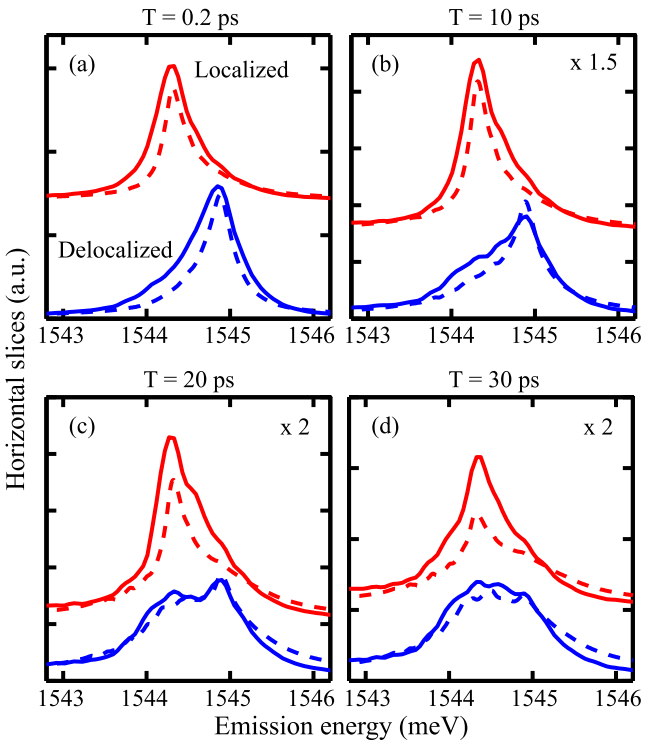

FIG. 8. (a)–(d) Horizontal slices from experimental and simulated 2D spectra for $T = 0.2$, 10, 20, and 30 ps, respectively, with the sample at a temperature of 5 K. The slices are for the excitation energies indicated in Figs. 6(a) and 7(a). The lower excitation energy slices are on the top and the higher excitation energy slices are on the bottom. The experimental and simulated slices are shown as solid and dashed lines, respectively. The simulated slices are scaled by the number indicated in the top right corner of the panels.

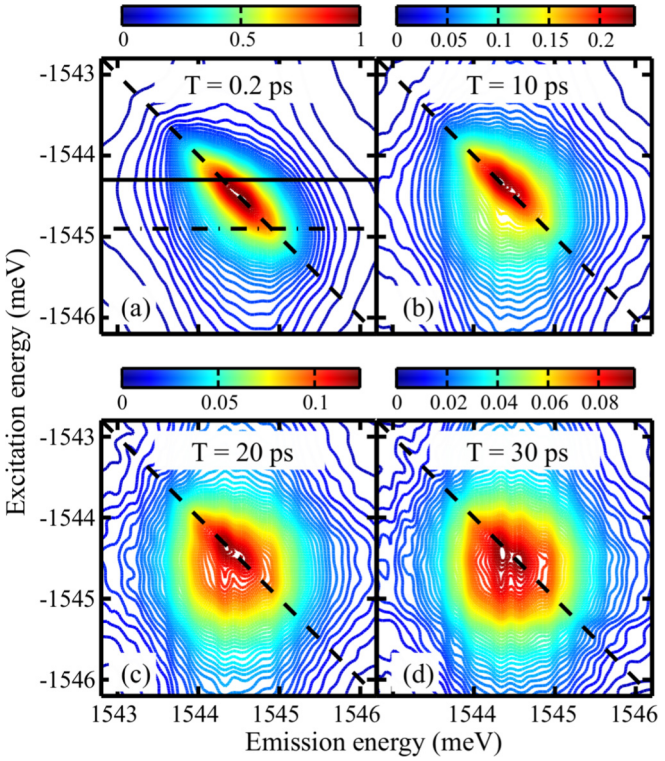

FIG. 9. (a)–(d) Experimental 2D spectra for $T = 0.2$, 10, 20, and 30 ps, respectively, with the sample at a temperature of 20 K. All the spectra are normalized by the maximum of the peak of the spectrum for $T = 0.2$ ps. The horizontal lines in (a) indicate excitation energies for the slices shown in Fig. 11.

a time scale longer than 10 ps, which is consistent with the time scale of exciton-phonon induced decay of delocalized exciton states close to the mobility edge [see Fig. 3(a)]. The influence of processes, which increase the exciton energy due to absorption of phonons, is weaker due to the small phonon population at this temperature [cf. Eq. (A2)]. The SRA, which assumes equal probability of increase and decrease in exciton energy, is not valid in this case. We emphasize that it is not possible to observe the time scale associated with this dynamic localization in either frequency-domain [35] or time-domain [25,26] FWM experiments that were previously used to study spectral diffusion in heterogeneous systems.

The excitation energy where the circled feature appears in Fig. 6(d) provides a clear indication of the energy at which the mobility edge appears, which is indicated in Fig. 1.

The simulated spectra shown in Fig. 7 reproduce the experimental findings qualitatively. We note that all the parameters for calculation of wave functions, microscopic coupling elements, and rates used in these simulations are consistent with previously published studies [40,41,52].

In the experimental and simulated data shown in Figs. 6 and 7, respectively, the different behavior of localized and delocalized excitons is apparent. However, to further highlight this distinction, we show in Fig. 8 two horizontal slices taken from the 2D spectra shown in Figs. 6 and 7; the excitation energies at which these slices have been taken are indicated in Figs. 6(a) and 7(a) by the solid and dashed horizontal lines. The spectral diffusion of localized and delocalized excitons is indicated by the change in the line shape of the low- and high-excitation-energy slices with increasing delay T. The evolutions of the localized and delocalized excitons, as shown in Fig. 8, are distinctly different: while the slice for localized excitons shows a narrow feature until 30 ps, the narrow feature is replaced by a broad peak ~20 ps for the delocalized-exciton slice. This behavior can be seen as a consequence of the phonon bottleneck of the localized states, which is visible as the decreased lifetime decay due to exciton-phonon scattering of the localized states compared to the delocalized states [cf. Fig. 3(a)].

Since exciton-phonon interactions are critical to spectral diffusion of excitons, we repeated the experiments at different temperatures. Figure 9 shows the 2D spectra measured for a sample temperature of 20 K and the same values of delay T as shown for 5 K in Fig. 6. We note that although the peak is still elongated along the diagonal direction, compared to the peak in Fig. 6(a), it is broader in the perpendicular direction due to increased dephasing arising from exciton-phonon scattering [53]. We find that the peak in this case is almost equally broadened for all excitation frequencies with increasing delay T; i.e., in addition to the relaxation of high-energy excitons to lower energies, the opposite process now is roughly equally probable due to an increased phonon population. The transition in spectral diffusion behavior is apparent at 20 K because the

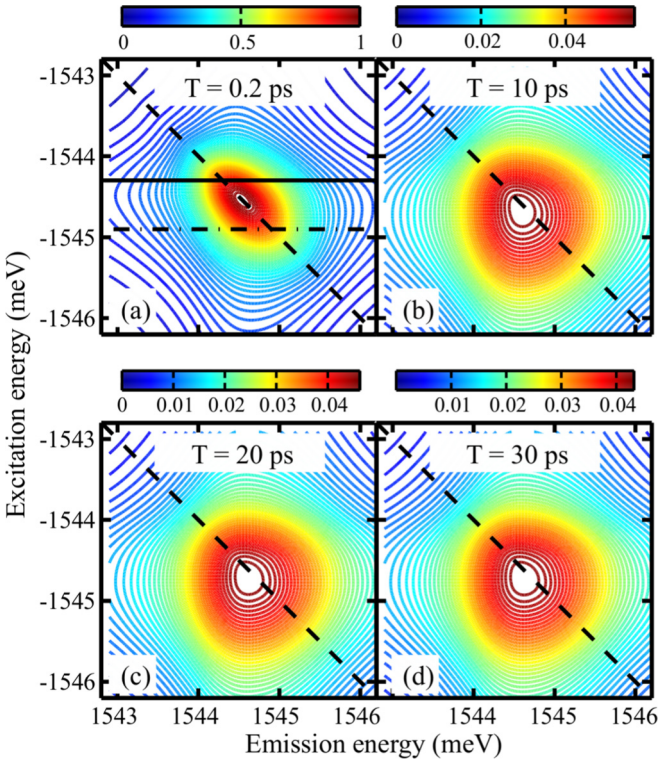

FIG. 10. (a)–(d) Simulated 2D spectra for $T = 0.2$, 10, 20, and 30 ps, respectively, with the sample at a temperature of 20 K. All the spectra are normalized by the maximum of the peak of the spectrum for $T = 0.2$ ps. The horizontal lines in (a) indicate excitation energies for the slices shown in Fig. 11.

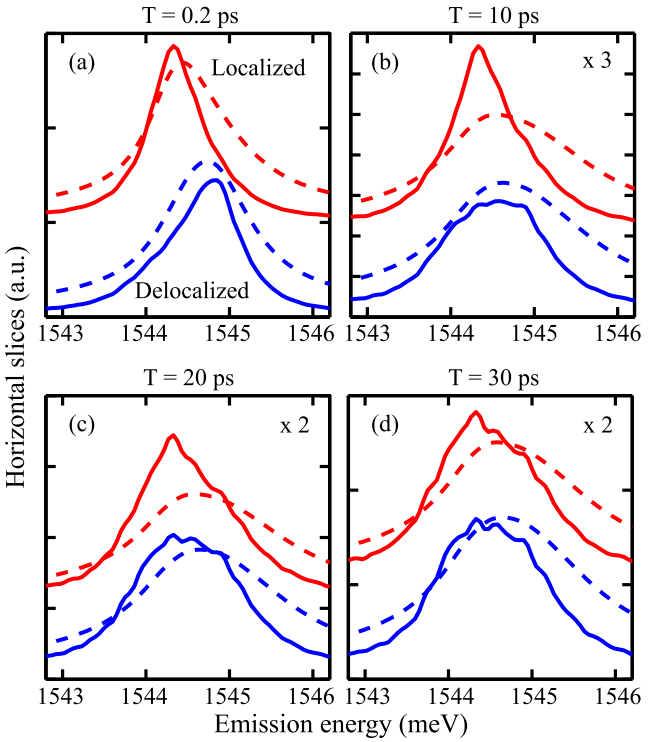

FIG. 11. (a)–(d) Horizontal slices from experimental and simulated 2D spectra for $T = 0.2$, 10, 20, and 30 ps, respectively, with the sample at a temperature of 20 K. The slices are for the excitation energies indicated in Figs. 9(a) and 10(a). The lower excitation energy slices are on the top and the higher excitation energy slices are on the bottom. The experimental and simulated slices are shown as solid and dashed lines, respectively. The simulated slices are scaled by the number indicated in the top right corner of the figures.

thermal energy is roughly equivalent to the energy needed to overcome the localization energy of ∼1.8 meV that we estimate for these QWs. The increase in exciton-phonon scattering for the exciton states, including the localized ones, is also reflected in the increased exciton-phonon decay rates in Fig. 3(b). This behavior is almost in agreement with the SRA, and is reproduced by the simulated spectra in Fig. 10, although the validity of the second-order Born-Markov exciton-phonon scattering is reduced at 20 K due to the increased importance of multiphonon processes, which are not included in our theory.

The transition to the SRA is also supported by the low- and high-excitation-energy slices shown in Fig. 11: both high- and low-excitation-energy slices become virtually identical by $T = 20$ ps in the experimental data. However, the difference between the two slices, especially those taken from experimental spectra, for shorter wait times suggests that even for this temperature, the low-energy excitons are somewhat localized in the sense that, compared to higher-energy excitons, they need more time to scatter to other states. Nonetheless, the phonon population in the bath is high enough that by 20 ps the final energy distribution of the exciton population is nearly independent of the initial energy at which excitons are created.

The gradual transition from dynamic localization at low sample temperature to the SRA at higher temperatures is highlighted by the 2D spectra measured for an intermediate sample temperature of 10 K, which are discussed in Appendix C.

B. Green's function

The change in exciton energy during spectral diffusion, as interpreted from the 2D spectra shown previously, is weighted by the transition dipole moments and broadened due to the homogeneous linewidths. The influence of these effects on spectral diffusion is not present in the simulated Green's functions, which we discuss next.

Figure 12 illustrates the evolution of the 2D probability map of the exciton effectively going from an initial state to any state at a final energy due to spectral diffusion at 5 K, with increasing delay T. The initial and final energies are perfectly correlated for $T = 0.2$ ps, as shown in Fig. 12(a). By $T = 30$ ps, however, inelastic exciton-phonon scattering has redistributed the exciton population to other energies as shown in Fig. 12(d). In particular, we find that the high-energy excitons preferentially relax to lower energy as indicated by the broad vertical feature around final energy of 1544.8 meV in Figs. 12(c) and 12(d). The strongly localized excitons below this energy have significant correlation between their initial and final energies, even for $T = 30$ ps due to the phonon bottleneck effect. Thus, spectral diffusion predominantly results in the dynamic localization of originally delocalized excitons. The scattering of excitons between localized sites [54] is relatively a much weaker effect at low

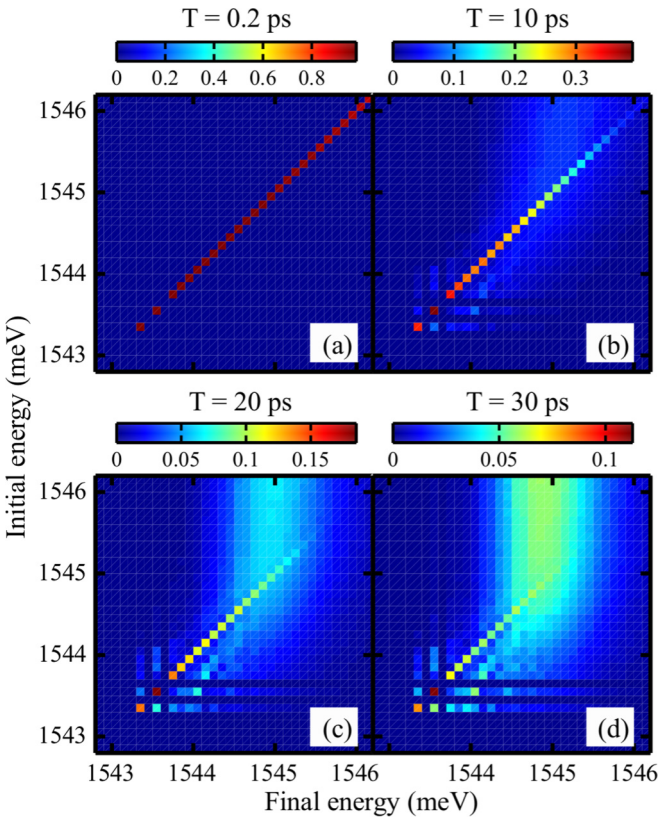

FIG. 12. (a)–(d) Simulated Green's function showing the probability distribution of change in the exciton energy for $T = 0.2$, 10, 20, 30 ps, respectively, at a sample temperature of 5 K after averaging for different realizations. Note that the vertical energy axes in these plots are oriented opposite to those in 2D spectra.

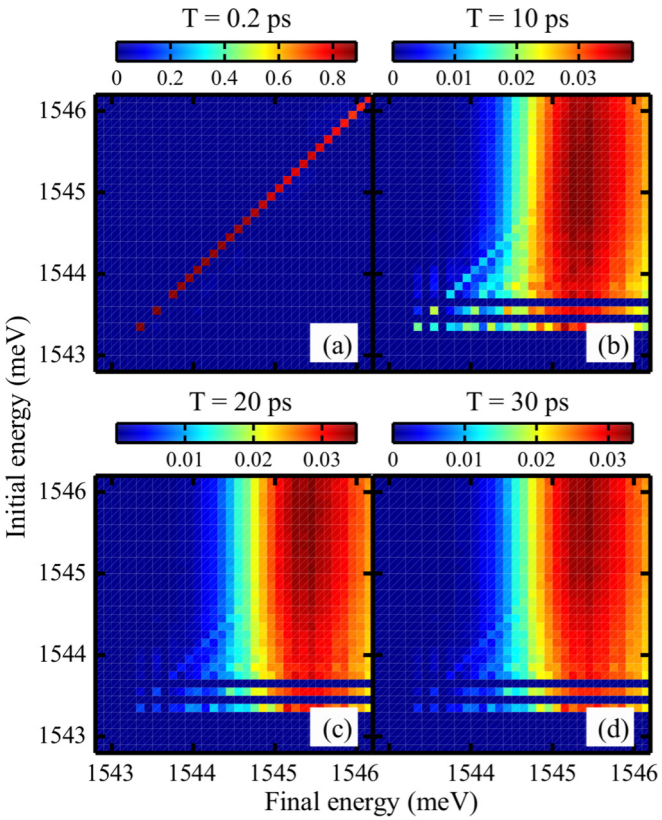

FIG. 13. (a)–(d) Simulated Green's function showing the probability distribution of change in the exciton energy for $T = 0.2$, 10, 20, 30 ps, respectively, at a sample temperature of 20 K after averaging for different realizations. Note that the vertical energy axes in these plots are oriented opposite to those in 2D spectra.

temperature, as indicated by the exciton-phonon decay rates in Fig. 3(a).

We also highlight the change in population distribution at 20 K through the Green's function simulations shown in Fig. 13. As expected from the measured 2D spectrum in Fig. 9(a), we find that the initial and final energies are well correlated for $T = 0.2$ ps in Fig. 13(a), which is similar to the behavior for the sample temperature of 5 K shown in Fig. 12(a). However, phonons with higher energy are thermally activated at 20 K and more scattering channels are opened. Consequently the initial and final energies are not correlated even for the low-energy (more localized) states for longer delays, as shown in Figs. 13(b)–13(d).

C. Dynamic localization

Now we will take a closer look at the process of dynamic localization for different sample temperatures and time delays. Using the calculated Green's function, we can define a measure for the dynamic localization of initially delocalized excitons to a particular final state as

$$P(E_f;T) = \frac{1}{\mathrm{DOS}(E_f)} \sum_{E_i=E_m}^{E_{\max}} G(E_f,E_i;T) \times \mathrm{DOS}(E_i), \tag{15}$$

where E_i and E_f are the initial and final exciton energies, respectively, $\mathrm{DOS}(E_j) = \sum_x \delta(E_x - E_j)$ is the density of states, E_m is the energy of the mobility edge, $E_{\max}$ is the maximum energy in the simulations, and G is the Green's function. Here the product in the summation gives a measure of the relaxation of a delocalized exciton to a final localized state. This value is then weighted by the density of states of the final exciton energy to get the relative likelihood of the localization process independently of the variation of the density of states with the exciton energy. The density of states and the energy of the mobility edge are the same as those shown in Fig. 1. We can also define the degree of localization of a given exciton state as

$$L(E) = \frac{R_{\max}}{R(E)}, \tag{16}$$

where E is the energy of the state, $R_{\max}$ is the simulation-area-limited maximum wave function size, and $R(E)$ is the size of the wave function of the state with energy E, as shown in Fig. 1.

Using the parameters defined above, we can look at the dependence of the likelihood of dynamic localization of initially delocalized excitons to a particular state on the degree of localization of the final state. Figure 14(a) shows the above dependence at different values of delay T for a sample temperature of 5 K. We find that the dynamic localization is

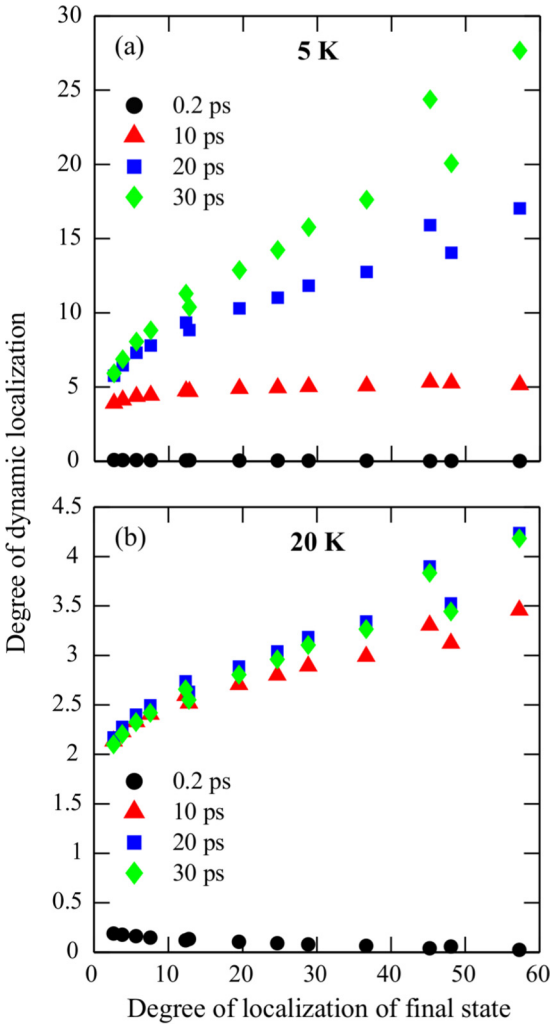

FIG. 14. Degree of dynamic localization to a particular final state as a function of the degree of localization of the final state for $T = 0.2$, 10, 20, and 30 ps, with the sample at a temperature of (a) 5 K and (b) 20 K.

significantly smaller for the first 10 ps than at later delays. These values are much higher for $T = 20$ and 30 ps. We also find that the likelihood of ending up in a particular state approximately scales linearly with the degree of localization of the final state. This behavior is a consequence of multiple scattering events during spectral diffusion. Thus, as the wait time increases, the excitons relax to a more localized state. This exciton relaxation is driven by the thermal distribution of phonons.

Similar data for a sample temperature of 20 K, presented in Fig. 14(b), however, shows a contrasting trend: the dynamic localization does not increase significantly with increasing wait times. This observation follows from the observation of spectral diffusion consistent with the SRA for a temperature of 20 K.

The quantitative data on dynamic localization presented in this section are consistent with the qualitative interpretation of measured 2D spectra discussed earlier. Additionally, it highlights the fact that the degree of localization increases with the increase in the localization of the final state.

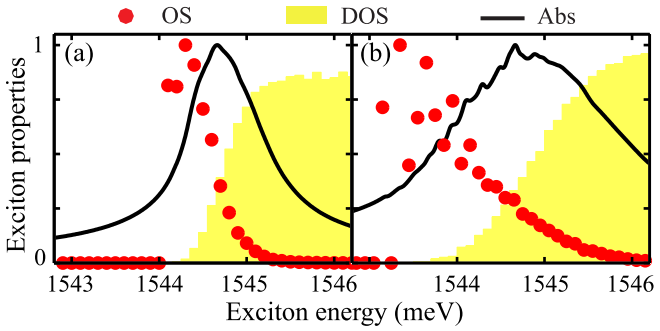

FIG. 15. Calculated oscillator strength (OS), density of states (DOS), and absorption spectrum (Abs) of the 1s-exciton resonance for disorder correlation lengths of (a) 10 nm and (b) 30 nm. The sample temperature was set at 5 K. The energy axis is shifted by the same amount as in Fig. 1.

D. Disorder correlation length

In this work so far, we have used a disorder correlation length $\xi = 20$ nm in our simulations, which provides a good match with the experimental results. However, the calculated spectral diffusion behavior is strongly dependent on this value. Presently, we will discuss the effect of the correlation length on the spectral diffusion characteristics.

The effect of the disorder correlation length on spectral diffusion can be intuitively understood through its effect on the excitonic properties shown in Figs. 15(a) and 15(b)

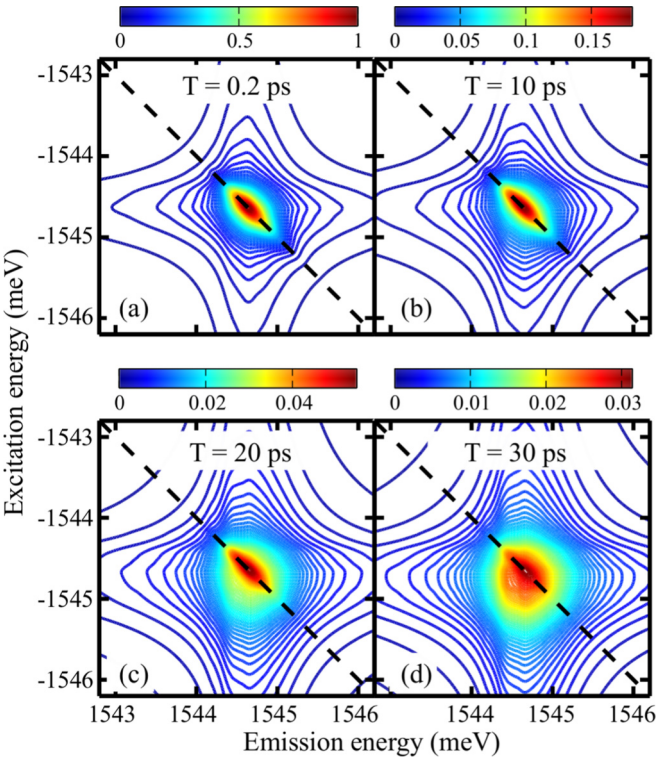

FIG. 16. (a)–(d) Simulated 2D spectra for $T = 0.2$, 10, 20, and 30 ps, respectively, with the sample at a temperature of 5 K using disorder correlation length $\xi = 10$ nm. All the spectra are normalized by the maximum of the peak of the spectrum for $T = 0.2$ ps.

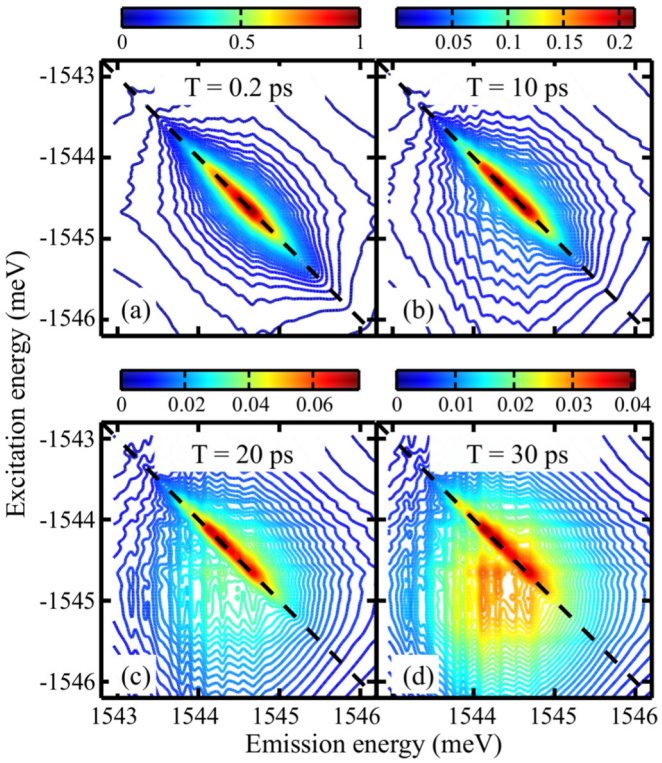

FIG. 17. (a)–(d) Simulated 2D spectra for $T = 0.2$, 10, 20, and 30 ps, respectively, with the sample at a temperature of 5 K using disorder correlation length $\xi = 30$ nm. All the spectra are normalized by the maximum of the peak of the spectrum for $T = 0.2$ ps.

for $\xi = 10$ and 20 nm, respectively. On comparing the two plots, we find that a decreased correlation length reduces the number of localized states. Furthermore, a faster decrease in the oscillator strength with increasing exciton energy is observed for smaller correlation length. As mentioned earlier, the absorption spectrum can be approximately treated as the product of the oscillator strength and the density of states. As a consequence, the inhomogeneous broadening of the exciton resonance increases with the disorder correlation length. This behavior is reflected in the increase in the width of the absorption spectrum with an increase in the disorder correlation length, as shown in Fig. 15.

Figures 16 and 17 show the simulated 2D spectra using $\xi = 10$ and 30 nm, respectively, for a sample temperature of 5 K. For a comparison with the results shown previously, we show the 2D spectra for the same waiting times. Due to an increase in the inhomogeneous broadening with an increase in the disorder correlation length, the 2D spectrum for $T = 0.2$ ps is significantly more elongated along the diagonal direction for $\xi = 30$ nm [Fig. 17(a)] than for $\xi = 10$ nm [Fig. 16(a)]. The increase in inhomogeneous broadening is also accompanied by a more obvious signature of dynamic localization of excitons. However the time scales of the localization process do not change considerably since they depend on the exciton-phonon scattering rates, which are almost independent of the correlation length.

V. CONCLUSION

In summary, we have measured the spectral diffusion of excitons in QWs, over the entire inhomogeneous distribution, using 2DCS for sample temperatures in the range 5–20 K. We find that the dynamic localization of excitons through emission of phonons is the dominant process at 5 K, and occurs over time scales of tens of picoseconds, which is illustrated by the simulated Green's function. At higher sample temperatures, redistribution of the exciton energy occurs uniformly to higher and lower energies due to an increase in the population of phonons. The simulated Green's function also allowed us to show that the degree of dynamic localization to a final state increases with an increase in its degree of localization. Finally, we also showed that the dynamic localization is more important for samples with higher disorder correlation length.

These results suggest that qualitatively similar exciton dynamics can be expected in other disordered semiconductors such as layered TMDs and perovskites. Interestingly, the exciton diffusion coefficient in atomically thin TMDs, which exhibit significantly larger inhomogeneous broadening and order-of-magnitude larger many-body interactions [55,56], is comparable to that for excitons in a GaAs QW [57,58] despite the fundamental difference in the nature of exciton localization [15]. 2DCS experiments may shed light on the limitations of exciton diffusion in these novel materials.

ACKNOWLEDGMENTS

This work was primarily supported by the Chemical Sciences, Geosciences, and Energy Biosciences Division, Office of Basic Energy Science, Office of Science, US Department of Energy, under Award No. DE5 FG02-02ER15346 and by the NSF under Grant No. 1125844. Financial support by Deutsche Forschungsgemeinschaft (DFG) through Sonderforschungsbereich 787 (Project B1) is gratefully acknowledged.

APPENDIX A: SCATTERING RATES

1. Radiative decay

In order to describe the dynamics of the density matrix elements, the scattering rates for the various excitation decay processes were calculated. One of these processes is the radiative recombination of the exciton to the ground state. We use the formulas from Ref. [41] for the limit of well-localized exciton states to obtain the radiative decay rate r_x for the exciton state x:

$$r_x = \frac{4}{3\hbar\varepsilon_B}|d_{cv}|^2\left|\phi_{1s}^2(0)\right|^2\frac{\omega_x^3}{n^3} \times \left|\int dR\,\psi_x(\mathbf{R})\right|^2\left|\int dz\,\zeta_e^*(z)\zeta_h(z)\right|^2, \quad \text{(A1)}$$

with d_{cv} being the dipole moment of the semiconductor intraband transitions, the transition frequency of the exciton ω_x, and the dielectric background constant ε_B, and the material refractive index n. For the more delocalized exciton states this formula overestimates the radiative decay slightly [41]. Since a qualitative agreement with the experiment is sufficient, this systematic error is not relevant for this work.

2. Exciton-phonon scattering

The second important scattering process is the exciton-phonon scattering within the manifold of different disorder states of the $1s$ exciton. We use the rates derived in Ref. [59], which uses the fact that the dominant quasimomentum transfer is in the z direction. For the scattering of exciton from state x to x', the applied formula has the form

$$\gamma_{x\to x'} = \frac{n(E_{x'}-E_x)(E_{x'}-E_x)}{\hbar^2 v_s^3 \rho}|D_c K_e(q_z) - D_v K_h(q_z)|^2 \int dR |\Psi_x(\mathbf{R})|^2 |\Psi_{x'}(\mathbf{R})|^2, \quad \text{(A2)}$$

with $q_z = |E_{x'} - E_x|/v_s$, $K_i(q_z) = \int dz \zeta_i^*(z)\zeta_i(z)e^{\imath q_z z}$, the speed of sound $v_s = 0.00370$ nm/fs [52], deformation potentials $D_v = -8.6$ eV and $D_c = 8.7$ eV for the valence and conduction bands, respectively [52], and density of GaAs $\rho = 5370\ \mathrm{kg/m^3}$.

APPENDIX B: PATHWAY CONTRIBUTIONS

We will now present the contribution of individual pathways shown in Fig. 5 to the FWM signal. The first coherent ESE contribution is

$$S_{\mathbf{k}_S,\mathrm{ESE}(a)}(\Omega_3,T,\Omega_1) = -\sum_{xx'} \mu_{x'g}^* \cdot \mathbf{E}_s^* \mu_{xg} \cdot \mathbf{E}_3 \mu_{x'g} \cdot \mathbf{E}_2 \mu_{xg}^* \cdot \mathbf{E}_1^* \times \frac{e^{-\imath\Theta_{x'x}T}}{\hbar^3(\Omega_3 - \Theta_{x'g})(\Omega_1 - \Theta_{gx})} \quad \text{(B1)}$$

with $\Theta_{ij} = E_i - E_j - \imath(\gamma_i + \gamma_j)$ and the dipole moments μ_{xg}. The dipole moments are proportional to the integral $\int dR \psi_n(\mathbf{R})$ for the corresponding COM wave function of the one-exciton states. Since we consider only the spectral dynamics within a very small spectral range, we neglected the influence of the pulse bandwidth.

The second ESE contribution features an incoherent population relaxation during delay T,

$$S_{\mathbf{k}_S,\mathrm{ESE}(b)}(\Omega_3,T,\Omega_1) = -\sum_{xx'} \mu_{x'g}^* \cdot \mathbf{E}_s^* \mu_{x'g} \cdot \mathbf{E}_3 \mu_{xg} \cdot \mathbf{E}_2 \mu_{xg}^* \cdot \mathbf{E}_1^* \times \frac{G_{x'x}(T)}{\hbar^3(\Omega_3 - \Theta_{x'g})(\Omega_1 - \Theta_{gx})}, \quad \text{(B2)}$$

which is incorporated through the relaxation Green's function $G_{x'x}(T)$.

Similar coherent and incoherent contributions are also visible in the ESA diagrams:

$$S_{\mathbf{k}_S,ESA(a)}(\Omega_3,T,\Omega_1) = \sum_{fxx'} \mu_{fx'}^* \cdot \mathbf{E}_s^* \mu_{fx'} \cdot \mathbf{E}_3 \mu_{x'g} \cdot \mathbf{E}_2 \mu_{xg}^* \cdot \mathbf{E}_1^* \times \frac{e^{-\imath\Theta_{x'x}T}}{\hbar^3(\Omega_3 - \Theta_{fx})(\Omega_1 - \Theta_{gx})}, \quad \text{(B3)}$$

$$S_{\mathbf{k}_S,ESA(b)}(\Omega_3,T,\Omega_1) = \sum_{fxx'} \mu_{fx}^* \cdot \mathbf{E}_s^* \mu_{fx'} \cdot \mathbf{E}_3 \mu_{xg} \cdot \mathbf{E}_2 \mu_{xg}^* \cdot \mathbf{E}_1^* \times \frac{G_{x'x}(T)}{\hbar^3(\Omega_3 - \Theta_{fx'})(\Omega_1 - \Theta_{gx})}. \quad \text{(B4)}$$

The dipole moment of the one-exciton to two-exciton states are related to μ_{gx}. For a two-exciton state f composed from two single excitons x_1, x_2, $\mu_{fx} = \delta_{xx_1}\mu_{x_2g} + \delta_{xx_2}\mu_{x_1g}$ within our approximations for non- or weakly interacting excitons.

The standard GSB diagram has the following form:

$$S_{\mathbf{k}_S,\mathrm{GSB}(a)}(\Omega_3,T,\Omega_1) = -\sum_{xx'} \mu_{x'g}^* \cdot \mathbf{E}_s^* \mu_{x'g} \cdot \mathbf{E}_3 \mu_{xg} \cdot \mathbf{E}_2 \mu_{xg}^* \cdot \mathbf{E}_1^* \times \frac{1}{\hbar^3(\Omega_3 - \Theta_{x'g})(\Omega_1 - \Theta_{gx})}. \quad \text{(B5)}$$

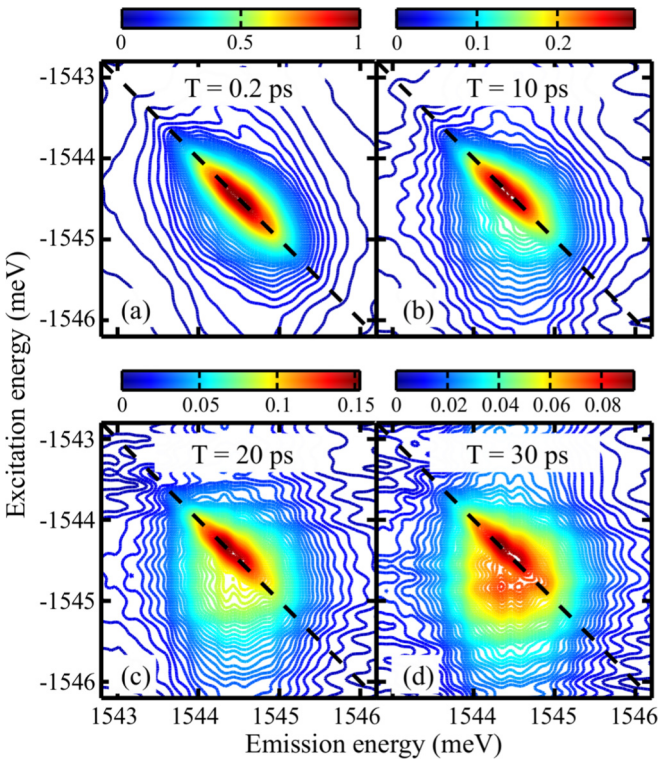

FIG. 18. (a)–(d) Experimental 2D spectra for $T = 0.2$, 10, 20, and 30 ps, respectively, with the sample at a temperature of 10 K. All the spectra are normalized by the maximum of the peak of the spectrum for $T = 0.2$ ps.

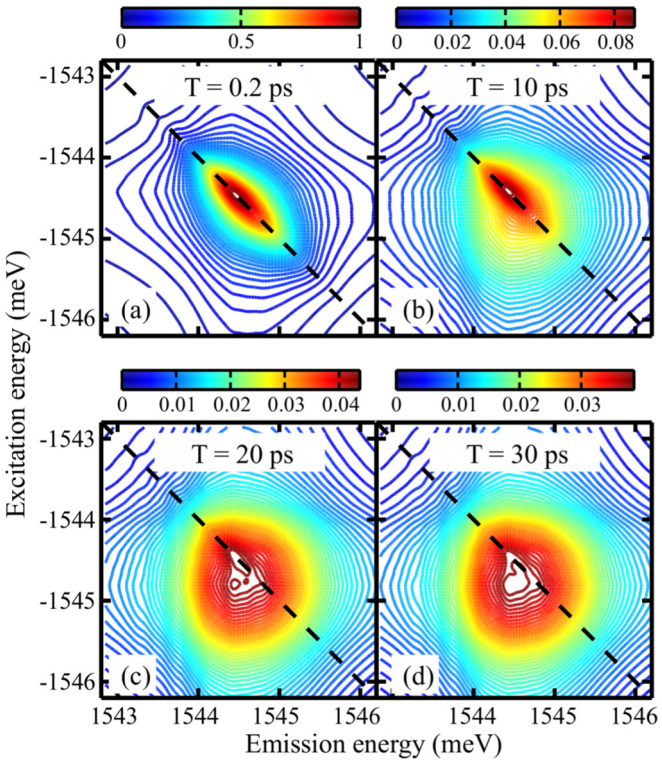

FIG. 19. (a)–(d) Simulated 2D spectra for $T = 0.2$, 10, 20, and 30 ps, respectively, with the sample at a temperature of 10 K. All the spectra are normalized by the maximum of the peak of the spectrum for $T = 0.2$ ps.

Besides this contribution, we also have a GSB contribution for the case the when the one-exciton population has decayed during delay T:

$$S_{\mathbf{k}_S,\mathrm{GSB}(b)}(\Omega_3, T, \Omega_1) = \sum_{xx'} \mu^*_{x'g} \cdot \mathbf{E}^*_s \mu_{x'g} \cdot \mathbf{E}_3 \mu_{xg} \cdot \mathbf{E}_2 \mu^*_{xg} \cdot \mathbf{E}^*_1 \times \frac{1 - \sum_{\tilde{x}} G_{x\tilde{x}}(\tau)}{\hbar^3(\Omega_3 - \Theta_{x'g})(\Omega_1 - \Theta_{gx})}, \quad \text{(B6)}$$

where $1 - \sum_{\tilde{x}} G_{x\tilde{x}}(\tau)$ represents the probability that the system is decayed to the ground state after time delay T starting from single-exciton state x.

APPENDIX C: DATA FOR INTERMEDIATE TEMPERATURE

We have shown that the SRA is clearly not valid for the sample at a temperature of 5 K. However, at the temperature of 20 K we find that spectral diffusion of excitons proceeds roughly as expected from the SRA. In order to highlight this transition, we show the 2D spectra for sample temperature of 10 K in Fig. 18. As expected, we find that the spectral diffusion characteristics for 10 K are intermediate between those observed for 5 and 20 K. Specifically, while the whole spectrum gets broader with increasing T, the peak shape is distinctly asymmetric for $T = 30$ ps [Fig. 18(d)]. Once again the simulated spectra qualitatively reproduce this behavior, as shown in Fig. 19.

[1] D. Sanvitto, F. Pulizzi, A. J. Shields, P. C. M. Christianen, S. N. Holmes, M. Y. Simmons, D. A. Ritchie, J. C. Maan, and M. Pepper, Science **294**, 837 (2001).

[2] P. G. Sionnest, J. Phys. Chem. Lett. **3**, 1169 (2012).

[3] O. V. Kozlov, F. de Haan, R. A. Kerner, B. P. Rand, D. Cheyns, and M. S. Pshenichnikov, Phys. Rev. Lett. **116**, 057402 (2016).

[4] F. Caruso, A. W. Chin, A. Datta, S. F. Huelga, and M. B. Plenio, J. Chem. Phys. **131**, 105106 (2009).

[5] H.-S. Kim, C.-R. Lee, J.-H. Im, K.-B. Lee, T. Moehl, A. Marchioro, S.-J. Moon, R. Humphry-Baker, J.-H. Yum, J. E. Moser, M. Grätzel, and N.-G. Park, Sci. Rep. **2**, 591 (2012).

[6] A. P. Kulkarni, C. J. Tonzola, A. Babel, and S. A. Jenekhe, Chem. Mater. **16**, 4556 (2004).

[7] J. M. Caruge, J. E. Halpert, V. Wood, V. Bulović, and M. G. Bawendi, Nat. Photonics **2**, 247 (2008).

[8] M. Liu, X. Yin, E. U. Avila, B. Geng, T. Zentgraf, L. Ju, F. Wang, and X. Zhang, Nature (London) **474**, 64 (2011).

[9] W. Hu, H. Nakashima, K. Furukawa, Y. Kashimura, K. Ajito, Y. Liu, D. Zhu, and K. Torimitsu, J. Am. Chem. Soc. **127**, 2804 (2005).

[10] G. Grosso, J. Graves, A. T. Hammack, A. A. High, L. V. Butov, M. Hanson, and A. C. Gossard, Nat. Photonics **3**, 577 (2009).

[11] G. Eytan, Y. Yayon, M. Rappaport, H. Shtrikman, and I. Bar-Joseph, Phys. Rev. Lett. **81**, 1666 (1998).

[12] D. S. Ginger and N. C. Greenham, J. Appl. Phys. **87**, 1361 (2000).

[13] N. Y. Morgan, C. A. Leatherdale, M. Drndić, M. V. Jarosz, M. A. Kastner, and M. Bawendi, Phys. Rev. B **66**, 075339 (2002).

[14] X. Wu, M. T. Trinh, D. Niesner, H. Zhu, Z. Norman, J. S. Owen, O. Yaffe, B. J. Kudisch, and X.-Y. Zhu, J. Am. Chem. Soc. **137**, 2089 (2015).

[15] A. Singh, G. Moody, K. Tran, M. E. Scott, V. Overbeck, G. Berghäuser, J. Schaibley, E. J. Seifert, D. Pleskot, N. M. Gabor, J. Yan, D. G. Mandrus, M. Richter, E. Malic, X. Xu, and X. Li, Phys. Rev. B **93**, 041401 (2016).

[16] C. Weisbuch, R. Dingle, A. Gossard, and W. Wiegmann, Solid State Commun. **38**, 709 (1981).

[17] S. B. Ogale, A. Madhukar, F. Voillot, M. Thomsen, W. C. Tang, T. C. Lee, J. Y. Kim, and P. Chen, Phys. Rev. B **36**, 1662 (1987).

[18] J. Hegarty and M. D. Sturge, J. Opt. Soc. Am. B **2**, 1143 (1985).

[19] Y. Takahashi, S. S. Kano, K. Muraki, S. Fukatsu, Y. Shiraki, and R. Ito, Appl. Phys. Lett. **64**, 1845 (1994).

[20] H. F. Hess, E. Betzig, T. D. Harris, L. N. Pfeiffer, and K. W. West, Science **264**, 1740 (1994).

[21] J. Hegarty, L. Goldner, and M. D. Sturge, Phys. Rev. B **30**, 7346 (1984).

[22] T. Takagahara, Phys. Rev. B **32**, 7013 (1985).

[23] X. Wu, M. T. Trinh, and X.-Y. Zhu, J. Phys. Chem. C **119**, 14714 (2015).

[24] H. Wang and D. G. Steel, Phys. Rev. A **43**, 3823 (1991).

[25] H. J. Bakker, K. Leo, J. Shah, and K. Köhler, Phys. Rev. B **49**, 8249 (1994).

[26] S. G. Carter, Z. Chen, and S. T. Cundiff, Phys. Rev. B **76**, 121303 (2007).
[27] The correlation function $C(T)$ is defined as $\langle \delta\omega(T)\delta\omega(0)\rangle$, where $\delta\omega(T)$ is the time-dependent difference between the resonance energy and its mean value.
[28] M. Cho, J.-Y. Yu, T. Joo, Y. Nagasawa, S. A. Passino, and G. R. Fleming, J. Phys. Chem. **100**, 11944 (1996).
[29] V. O. Lorenz and S. T. Cundiff, Phys. Rev. Lett. **95**, 163601 (2005).
[30] V. O. Lorenz, S. Mukamel, W. Zhuang, and S. T. Cundiff, Phys. Rev. Lett. **100**, 013603 (2008).
[31] M. Maroncelli and G. R. Fleming, J. Chem. Phys. **86**, 6221 (1987).
[32] R. Jimenez, G. R. Fleming, P. V. Kumar, and M. Maroncelli, Nature (London) **369**, 471 (1994).
[33] S. A. Empedocles, D. J. Norris, and M. G. Bawendi, Phys. Rev. Lett. **77**, 3873 (1996).
[34] H. D. Robinson and B. B. Goldberg, Phys. Rev. B **61**, R5086 (2000).
[35] H. Wang and D. Steel, Appl. Phys. A **53**, 514 (1991).
[36] R. Singh, G. Moody, M. E. Siemens, H. Li, and S. T. Cundiff, J. Opt. Soc. Am. B **33**, C137 (2016).
[37] Y. Ogawa, H. Tahara, and F. Minami, Phys. Rev. B **87**, 165305 (2013).
[38] M. T. Zanni, M. C. Asplund, and R. M. Hochstrasser, J. Chem. Phys. **114**, 4579 (2001).
[39] J. D. Hybl, A. Yu, D. A. Farrow, and D. M. Jonas, J. Phys. Chem. A **106**, 7651 (2002).
[40] R. Zimmermann, F. Grosse, and E. Runge, Pure Appl. Chem. **69**, 1179 (1997).
[41] R. Zimmermann, E. Runge, and V. Savona, in *Quantum Coherence Correlation and Decoherence in Semiconductor Nanostructures*, edited by T. Takagahara (Academic Press Inc., San Diego, 2003), pp. 89–165.
[42] S. Balay, S. Abhyankar, M. F. Adams, J. Brown, P. Brune, K. Buschelman, L. Dalcin, V. Eijkhout, W. D. Gropp, D. Kaushik, M. G. Knepley, L. C. McInnes, K. Rupp, and B. F. Smith, PETSc Web page, http://www.mcs.anl.gov/petsc.
[43] S. Balay, S. Abhyankar, M. F. Adams, J. Brown, P. Brune, K. Buschelman, L. Dalcin, V. Eijkhout, W. D. Gropp, D. Kaushik, M. G. Knepley, L. C. McInnes, K. Rupp, and B. F. Smith, PETSc Users Manual, Tech. Rep. ANL-95/11, Revision 3.6, Argonne National Laboratory, 2015.
[44] S. Balay, W. D. Gropp, L. C. McInnes, and B. F. Smith, in *Modern Software Tools in Scientific Computing*, edited by E. Arge, A. M. Bruaset, and H. P. Langtangen (Birkhäuser Press, Boston, 1997), pp. 163–202.
[45] V. Hernandez, J. E. Roman, and V. Vidal, ACM Trans. Math. Software **31**, 351 (2005).
[46] B. Fornberg and D. M. Sloan, Acta Numerica **3**, 203 (1994).
[47] A. D. Bristow, D. Karaiskaj, X. Dai, R. P. Mirin, and S. T. Cundiff, Phys. Rev. B **79**, 161305 (2009).
[48] Although we assumed that the coupling between the different exciton states with different COM motion is negligible, our formalism included the two-exciton states. Doing so makes it straightforward to include situations where the above assumption might not be valid, as in the case of double quantum coherence experiments [60,61].
[49] A. D. Bristow, D. Karaiskaj, X. Dai, T. Zhang, C. Carlsson, K. R. Hagen, R. Jimenez, and S. T. Cundiff, Rev. Sci. Instrum. **80**, 073108 (2009).
[50] G. Moody, M. E. Siemens, A. D. Bristow, X. Dai, A. S. Bracker, D. Gammon, and S. T. Cundiff, Phys. Rev. B **83**, 245316 (2011).
[51] D. Abramavicius, B. Palmieri, D. V. Voronine, F. Sanda, and S. Mukamel, Chem. Rev. **109**, 2350 (2009).
[52] U. Bockelmann, Phys. Rev. B **48**, 17637 (1993).
[53] J. Lee, E. S. Koteles, and M. O. Vassell, Phys. Rev. B **33**, 5512 (1986).
[54] T. Takagahara, J. Lumin. **44**, 347 (1989).
[55] G. Moody, C. K. Dass, K. Hao, C.-H. Chen, L.-J. Li, A. Singh, K. Tran, G. Clark, X. Xu, G. Berghauser, E. Malic, A. Knorr, and X. Li, Nat. Commun. **6**, 8315 (2015).
[56] A. Chernikov, T. C. Berkelbach, H. M. Hill, A. Rigosi, Y. Li, O. B. Aslan, D. R. Reichman, M. S. Hybertsen, and T. F. Heinz, Phys. Rev. Lett. **113**, 076802 (2014).
[57] D. Oberhauser, K.-H. Pantke, J. M. Hvam, G. Weimann, and C. Klingshirn, Phys. Rev. B **47**, 6827 (1993).
[58] Q. Cui, F. Ceballos, N. Kumar, and H. Zhao, ACS Nano **8**, 2970 (2014).
[59] R. Zimmermann and E. Runge, Phys. Status Solidi A **164**, 511 (1997).
[60] D. Karaiskaj, A. D. Bristow, L. Yang, X. Dai, R. P. Mirin, S. Mukamel, and S. T. Cundiff, Phys. Rev. Lett. **104**, 117401 (2010).
[61] X. Dai, M. Richter, H. Li, A. D. Bristow, C. Falvo, S. Mukamel, and S. T. Cundiff, Phys. Rev. Lett. **108**, 193201 (2012).